Partial Order-Disorder Transition Driving Closure of Band Gap: Example of Thermoelectric Clathrates

Maria Troppenz,[1,*] Santiago Rigamonti,[1] Jorge O. Sofo,[2] and Claudia Draxl[1]
[1]Institut für Physik und Iris Adlershof, Humboldt-Universität zu Berlin, Zum Großen Windkanal 2, 12489 Berlin, Germany
[2]Department of Physics and Materials Research Institute, The Pennsylvania State University, University Park, Pennsylvania 16802, USA

(Received 18 September 2020; revised 14 February 2023; accepted 24 March 2023; published 21 April 2023)

In the quest for efficient thermoelectrics, semiconducting behavior is a targeted property. Yet, this is often difficult to achieve due to the complex interplay between electronic structure, temperature, and disorder. We find this to be the case for the thermoelectric clathrate $Ba_8Al_{16}Si_{30}$: Although this material exhibits a band gap in its ground state, a temperature-driven partial order-disorder transition leads to its effective closing. This finding is enabled by a novel approach to calculate the temperature-dependent effective band structure of alloys. Our method fully accounts for the effects of short-range order and can be applied to complex alloys with many atoms in the primitive cell, without relying on effective medium approximations.

DOI: 10.1103/PhysRevLett.130.166402

Disorder is a frequent phenomenon in materials used in technologically relevant applications. It affects key properties, in particular the electronic band structure that, in turn, determines electron and heat transport and more. Devising concepts for calculating the energy spectrum in the presence of disorder has a long history, including effective-medium theories such as the virtual-crystal approximation [1], the coherent-potential approximation [2,3], and extensions thereof [4]. However, comprehensive consideration of systems with large numbers of atoms in their primitive cell, where local-environment effects are important, has challenged these techniques [4,5].

In this Letter, we address this problem and demonstrate a method to compute the finite-temperature effective band structure of alloys. A combination of the cluster expansion (CE) [6] with the Wang-Landau (WL) [7] method is employed to obtain an ensemble-averaged effective band structure from first principles. Our approach allows for uncovering the interplay between temperature-dependent alloy disorder and the related electronic properties. Atom relaxations and dopant-dopant correlations, leading to short-range order, are incorporated by construction. We demonstrate our method with the example of a complex thermoelectric alloy, namely, the intermetallic clathrate $Ba_8Al_{16}Si_{30}$. This composition is highly relevant since its ground state is a semiconductor [8], as desired for thermoelectricity. For this system, we observe a temperature-driven closing of its effective band gap, concomitant with a partial order-disorder transition at $T_c = 582$ K. Since conductance by p- or n-type doping is beneficial for thermoelectricity, the appearance of metallicity in the alloy may have a degrading effect on the expected thermoelectric efficiency.

Our method enables the calculation of the electronic energy spectrum at finite temperatures from a canonical ensemble average as follows. (i) For the composition of interest, we generate a set of configurations whose energies and electronic properties are determined by *ab initio* calculations. The number of configurations in the set is much smaller than the actual number of available configurations. (ii) For each configuration in the set, we restore the symmetry of the pristine primitive cell by an averaging procedure according to Refs. [9–11]. This symmetrized energy spectrum accounts for the different local environments present due to substitutents. (iii) The configurational density of states $g(E)$ is evaluated by canonical Wang-Landau sampling [7,12]. To predict the energy of the configurations visited during the sampling, we employ a CE model. (iv) Using $g(E)$, we assign a statistical weight to the symmetrized energy spectra from step (ii) and perform a canonical-ensemble average. The result is the finite-temperature effective band structure. For this average, the underlying assumption is spatial ergodicity [13]; i.e., all possible configurations in a finite sample are realized in the infinite sample. Thus, an average of many single finite samples can approximate the behavior of the infinite sample.

This method is applied, in the following, to calculate the finite-temperature effective band structure for the clathrate $Ba_8Al_{16}Si_{30}$. Intermetallic clathrates are inclusion compounds that encapsulate guest atoms inside cavities in their crystal lattice (see Fig. 1). The enormous compositional space for their synthesis offers, in principle, an excellent playground for tailoring their properties toward a high thermoelectric performance. The host structure of type-I clathrate compounds, consisting of 46 tetrahedrally

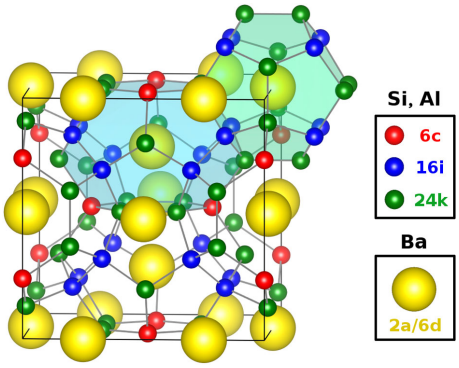

FIG. 1. Unit cell of the type-I clathrate structure $Ba_8Al_xSi_{46-x}$ (space group $Pm\bar{3}n$). Host atoms are at the Wyckoff sites of the pristine lattice, $w = 24k$ (green), $16i$ (blue), and $6c$ (red), guest atoms at $2a$ and $6d$ (yellow). Two guest-containing cavities are shown in light blue and light green.

coordinated group-IV species in the unit cell, can contain up to eight guest atoms, often alkali or alkaline-earth metals. These act as endohedral dopants and donate their outer-shell electrons. Following the Zintl rule [14], the compound $Ba_8Al_xSi_{46-x}$, with Ba as guest atoms and Al atoms doping the Si host (unit cell shown in Fig. 1), is expected to be charge balanced for $x = 16$ [15–17] thus semiconducting, while compositions below $x = 16$ are metallic. Indeed, previous studies have shown that the most stable structure of $Ba_8Al_{16}Si_{30}$ is a semiconductor [8]. However, also the arrangement of Al atoms in the host lattice plays an essential role in determining the electronic properties. In fact, it has been observed in several clathrate compounds that the electronic structure is very sensitive to subtle changes in the configuration [8,18–21]. In particular, configurations of $Ba_8Al_{16}Si_{30}$ with energies only a few meV/atom above the ground state are found to be metallic [8]. This poses a challenging scenario for a reliable theoretical description of such materials at finite temperatures, since, on the one hand, the properties of a single configuration (e.g., the lowest-energy structure) cannot represent the thermal average while, on the other hand, supercell sizes needed to describe the thermodynamic limit are out of reach.

To employ the described approach, we start by calculating the electronic properties of 44 $Ba_8Al_{16}Si_{30}$ configurations *ab initio* with the exchange-correlation functional PBEsol [22] by using the full-potential all-electron density functional theory (DFT) package `exciting` [23] [step (i); for details see the Supplemental Material (SM) [24]]. In this system, the unit cell consisting of 54 atoms is already sufficiently large to account for the effects of short-range correlations in the electronic structure. The fundamental DFT band gaps E_{gap} of the computed configurations with total energies below 21 meV/atom are shown in Fig. 2(a) (black dots, right-hand axis) where the ground-state (GS) energy E_{GS} serves as a reference (see Sec. I of the SM [24]).

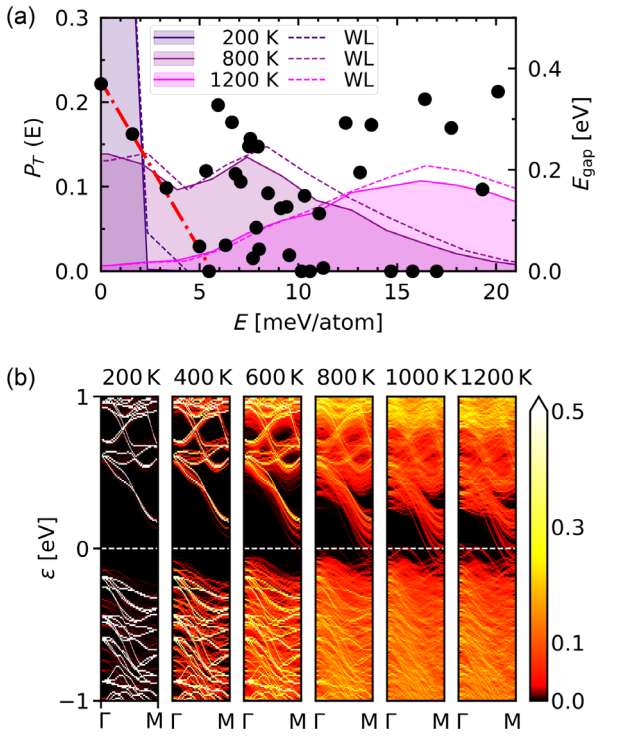

FIG. 2. (a) Canonical distribution $P_T(E)$ for $T = 200$, 800, and 1200 K (left axis) and Kohn-Sham band gaps E_{gap} (black dots, right axis) versus total energy E. The energy zero is the ground-state energy E_{GS}. The results for $P_T(E)$ obtained from the MC method are shown with shaded areas, those from the WL method with dashed lines. The linear decrease of the band gap at low energies is indicated by a red dash-dotted line. (b) Spectral function along the path Γ-M for temperatures between 200 and 1200 K (from left to right). The white dashed lines indicate the Fermi energy E_F. Black corresponds to $A_T(\boldsymbol{k}, \epsilon) = 0$, and white to $A_T(\boldsymbol{k}, \epsilon) > 0.5$.

The GS has an indirect band gap of 0.36 eV [8] along the Γ-M direction. Starting from this value, the band gap decreases almost linearly for configurations of increasing energy (red dash-dotted line) until becoming zero at around 5 meV/atom. For larger total energies, both semiconducting and metallic structures are present.

In step (ii), we calculate the symmetrized energy spectrum in the pristine primitive cell, i.e., that of the nonsubstituted clathrate lattice, for each of the 44 configurations. Because of the Al substituents, the symmetry of this cell is broken, such that the eigenvalues for the wave vectors $\boldsymbol{k}$ and $\boldsymbol{k}_S = S\boldsymbol{k}$, with S being a point symmetry operation of the primitive cell, are in general different. We average the energy spectrum over all point symmetry operations of the pristine lattice by defining a spectral function:

$$A_c(\boldsymbol{k}, \epsilon) = \frac{1}{N_S} \sum_S \sum_n \delta_\xi(\epsilon - \epsilon_{c,n\boldsymbol{k}_S}). \tag{1}$$

Here, $\epsilon_{c,n\boldsymbol{k}}$ is the eigenenergy of band n and wave vector $\boldsymbol{k}$ for configuration c. $\delta_\xi(x) = 1$ if $x \in [-\xi, \xi)$ and 0 otherwise. ξ is a small number representing the discretization of ϵ [y axis

in Fig. 2(b)]. In our case, an unfolding of the band structure to recover the translational symmetry of the primitive cell [9,11] is not required, since the lattice of the configurations has the same size as the latter. The symmetry-averaged spectral functions are shown for the GS and for high-energy structures in Figs. 1 and 2 of the SM [24].

Using the $A_c(\boldsymbol{k},\epsilon)$'s of the configurations with energies E_c, we can perform a canonical-ensemble average to obtain the finite-temperature spectral function $A_T(\boldsymbol{k},\epsilon)$:

$$A_T(\boldsymbol{k},\epsilon) \approx \frac{1}{Z_T}\sum_c A_c(\boldsymbol{k},\epsilon)e^{-E_c/k_BT}. \quad (2)$$

Here, the sum runs on the configurations c of the alloy with energy E_c and Z_T is the canonical partition function $Z_T = \sum_c e^{-E_c/k_BT}$. k_B is the Boltzmann constant. For sparse configurational samplings, the weight of different configurations in Eq. (2) may be misrepresented. To alleviate this problem, we employ the configurational density of states $g(E)$ obtained by the Wang-Landau sampling [7,12] [step (iii), shown in Fig. 3 in the SM [24]]. It is calculated with the cluster-expansion package CELL [25,26], using the CE model from Ref. [8] for predicting the energy of the configurations visited in the sampling.

After having obtained these statistical weights, $g(E)$, as a function of the energy E, the sum over the configurations c in Eq. (2) can be recast into a sum over energy intervals as (see Sec. II in the SM [24]):

$$A_T(\boldsymbol{k},\epsilon) = \frac{1}{Z_T}\sum_{i=0}^{M}\langle A_c(\boldsymbol{k},\epsilon)\rangle_i \Delta_i g(E_i)e^{-E_i/k_BT}. \quad (3)$$

This canonical-ensemble average yields the energy spectrum at finite temperature [step (iv)]. Here, $\langle A_c(\boldsymbol{k},\epsilon)\rangle_i = \sum_{c\in\Delta_{E_i}} A_c(\boldsymbol{k},\epsilon)/n_i$ is the configuration-averaged spectral weight in the interval $\Delta_{E_i} = [E_i, E_i+\Delta_i)$, with Δ_i being small interval widths. n_i is the number of computed configurations in Δ_{E_i}, while the total number of configurations in the same interval is $\Delta_i g(E_i)$, and $Z_T = \sum_i^M \Delta_i g(E_i)e^{-E_i/k_BT}$. The finite-temperature effective band structure resulting from the $A_T(\boldsymbol{k},\epsilon)$'s is shown in Fig. 2(b). At $T \leq 400$ K, there is a small indirect effective band gap between the valence band maximum close to the Γ point and the conduction band minimum at the M point. With increasing temperature, the effective band gap starts to decrease, and above 600 K, the spectral function at the Fermi energy becomes nonzero. This indicates a possible metallic state, given that no electron localization occurs (and we note that such effects are beyond the current theoretical description). The narrowing of the effective band gap with increasing temperature is also evident from the temperature-dependent density of states, as defined in the SM [24], which is shown for $200 \leq T \leq 1200$ K in Fig. 3(a). Here, the effective band gap closes at around 700 K.

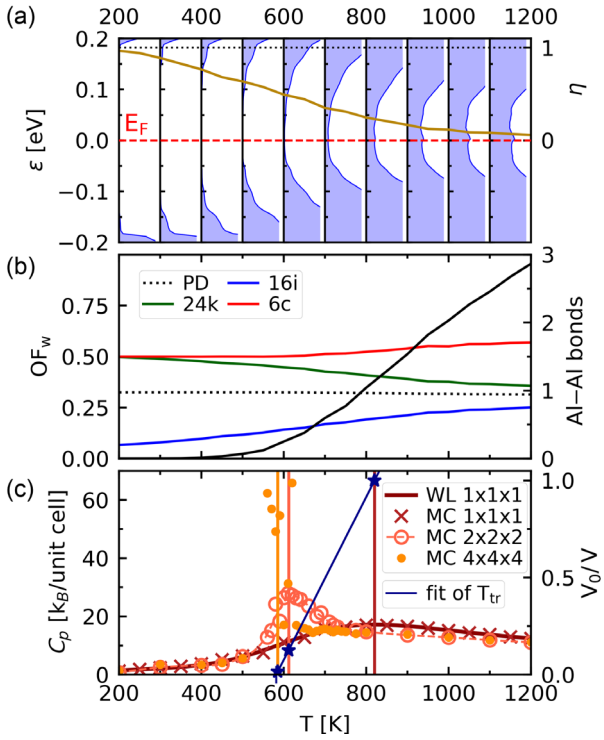

FIG. 3. Signatures of the phase transition. (a) Electronic density of states (blue shaded area, left axis; the Fermi level is indicated with a dashed red line) and order parameter η from Eq. (4) (brown line, right axis). (b) Occupation factors of the three Wyckoff sites 24k, 16i, 6c, and OF_{PD} (left axis), and number of Al—Al bonds (black line, right axis). (c) Specific heat C_p (left axis) for the $1\times1\times1$ cell obtained from the WL method (dark red solid line) and from the MC method (dark red crosses). In addition, C_p is shown for the $2\times2\times2$ (dashed orange line, circles) and $4\times4\times4$ (yellow dots) supercells from MC simulations. The transition temperatures T_{tr} are indicated by vertical lines of the corresponding color. The dark blue stars indicate the inverse of the supercell volume V^{-1} (right axis). The least-squares fit of Eq. (5) (dark blue solid line) to these data points yields a slope of $a = 238.4$ K V_0 and the transition temperature in the macroscopic limit, $T_{tr}(\infty) = 582$ K.

It is interesting to explore the structural and thermodynamic properties along this transition of band-gap closure. To this extent, we use the CE model of Ref. [8] to perform a configurational thermodynamics analysis of the system by means of finite-temperature canonical Metropolis Monte Carlo (MC) simulations [38,39]. Figure 2(a), left-hand axis, shows the canonical probability distribution from the MC method (solid lines). For $T = 200$ K, $P_T(E)$ has a single peak below 3 meV/atom. In this energy range, only semiconducting configurations are present. With increasing temperature, $P_T(E)$ becomes more pronounced in the region with metallic configurations (above 5 meV/atom). At 800 K, the probability distribution shows two maxima, one around 2 meV/atom and one around 8 meV/atom, signaling the coexistence of two phases. For $T = 1200$ K, the distribution becomes broader with a

single maximum at high energies. Similar results are obtained from the WL method using the expression $P_T(E) = g(E)e^{-E/k_BT}/Z_T$ (dashed lines).

To assess the dopant configurations, the Al occupancy factors, $\mathrm{OF}_w(T)$, are shown in Fig. 3(b). $\mathrm{OF}_w(T)$ is defined as the fractional number of Al atoms at the Wyckoff site w, with $w = 24k$, $16i$, or $6c$ (see Fig. 1). At $T \leq 200$ K, the OFs are almost identical to those of the ground-state configuration, that has 12, 1, and 3 Al atoms at the $24k$, $16i$, and $6c$ site, respectively (i.e., $\mathrm{OF}_{24k} = 0.5$, $\mathrm{OF}_{16i} = 0.0625$, and $\mathrm{OF}_{6c} = 0.5$), and lacks Al—Al bonds [8]. OF_{6c} remains almost constant over the full temperature range. At $T = 1200$ K, $\mathrm{OF}_{6c} = 0.57$, i.e., ~0.4 Al atoms more than the GS. In contrast, OF_{24k} decreases and OF_{16i} increases with temperature. At $T \approx 1200$ K, the number of Al—Al bonds has increased considerably (black line), where approximately 3.5 Al atoms have been transferred from the $24k$ to the $16i$ sublattice, approaching the value of partial disorder (PD), calculated as $\mathrm{OF}_{\mathrm{PD}}(T) = [16 - \mathrm{OF}_{6c}(T) \times 6]/40$ [black dotted line in Fig. 3(b)]. This value corresponds to a partially disordered structure, in which the sublattice formed by the $24k$ and $16i$ positions hosts a fully random Al-Si alloy. Since the actual Al content in the $24k$-$16i$ sublattice depends on the occupation of the $6c$ site, $\mathrm{OF}_{\mathrm{PD}}(T)$ is slightly temperature dependent, changing from 0.325 at 200 K to 0.315 at 1200 K.

The phase transition from a well-ordered state at low temperatures to a partially disordered state at high temperatures can be characterized by an order parameter [40,41] that we define such to be able to distinguish between these two phases:

$$\eta(T) = \frac{1}{2} \sum_{w=24k,16i} \left[\frac{\mathrm{OF}_w(T) - \mathrm{OF}_{\mathrm{PD}}(T)}{\mathrm{OF}_w(0\ \mathrm{K}) - \mathrm{OF}_{\mathrm{PD}}(0\ \mathrm{K})} \right]^2. \quad (4)$$

Per definition, it is exactly one for the ordered phase at 0 K, and becomes zero for the perfectly PD phase. Accordingly, it decreases from ~1 at 200 K to almost zero at 1200 K, as shown in Fig. 3(a) (brown line).

To determine the transition temperature T_{tr}, we investigate its signatures on the canonical probability distribution $P_T(E)$ and the isobaric specific heat $C_p(T) = (\langle E^2 \rangle - \langle E \rangle^2)/k_BT^2$. For first-order phase transitions, $P_T(E)$ at T_{tr} is expected to display two peaks with equal height [7,42], and C_p is expected to exhibit a maximum at the transition temperature [42–45]. As evident from Fig. 2(a), a double peak structure in $P_T(E)$ with nearly equal peak heights is, indeed, observed for a temperature of about 800 K. The results for $C_p(T)$ are shown in Fig. 3(c) for simulations using different supercell sizes. For a $1 \times 1 \times 1$ cell, C_p has a maximum at 820 K (indicated by the dark red vertical line), and both WL and MC simulations yield indistinguishable results.

Because of the finite size of the simulation cell, the computed value of T_{tr} deviates systematically from the macroscopic limit [42,43]. The transition temperature is expected to change linearly with the inverse of the simulation-cell volume V^{-1} [42,43] as

$$T_{\mathrm{tr}}(V) = T_{\mathrm{tr}}(\infty) + aV^{-1}. \quad (5)$$

Here, $T_{\mathrm{tr}}(\infty)$ is the transition temperature in the macroscopic limit and a is a constant. To determine $T_{\mathrm{tr}}(\infty)$, we calculate T_{tr} for a $2 \times 2 \times 2$ and a $4 \times 4 \times 4$ supercell, i.e., $V = 8V_0$ and $64V_0$, respectively (V_0 being the unit-cell volume), and fit Eq. (5) to these data points. For the $2 \times 2 \times 2$ supercell, we obtain $T_{\mathrm{tr}} = 621$ K from the maximum of C_p [see Fig. 3(c), circles]. For increasing supercell sizes, very large times are required to sample the distribution effectively close to the transition temperature [42,43,46]. This leads to an increased uncertainty of the computed C_p values, as can be seen for the $4 \times 4 \times 4$ supercell around $T = 600$ K [Fig. 3(c), dots], hampering an accurate determination of the peak position. Nonetheless, from a direct inspection of the MC trajectories for temperatures between 560 and 610 K, we see that the bimodal character of $g(E)$ leads to a sudden jump between low-energy and high-energy configurations at $T_{\mathrm{tr}} \approx 585$ K (see Fig. 4 of the SM [24]). We take this value as a reasonable estimate of T_{tr} for the $4 \times 4 \times 4$ supercell. The respective values of T_{tr} are indicated by vertical lines in Fig. 3(c). By performing a least-squares fit of Eq. (5) to the T_{tr}'s for the three supercell sizes [Fig. 3(c), dark blue solid line], we obtain $T_{\mathrm{tr}}(\infty) = 582$ K. This temperature differs significantly from T_{tr} of the unit cell, emphasizing the need of a finite-size scaling. We also see that with increasing cell size the peak of C_p increases in height and decreases in width, as typically observed for first-order phase transitions [42,44].

A further cross-check for a first-order transition is the temperature-dependent behavior of the entropy, where an inflection point at T_{tr} in the microcanonical ensemble is a necessary condition [27]. We, indeed, verify this behavior as obvious in Fig. 6 of the SM [24].

Finally, we carefully consider the effects of (a) thermal expansion, (b) vibrational free energy, and (c) electron-phonon coupling on the transition. For (a) we find that the change of the energy spectrum due to thermal expansion is negligible (see Sec. VI of the SM [24]). Considering (b), configurational disorder and lattice vibrations are linked by the vibrational entropy contribution to the free energy, since the latter may affect the relative stability of different configurations. For $T \leq 900$ K, we find this contribution to be less than 20% of the total free-energy differences, thus playing a minor role in the thermodynamic stability (see Sec. VII of the SM [24]). For (c), we employ the special displacement method [28,29] to compute the band-gap renormalization due to electron-phonon coupling (see Sec. VII of the SM [24]). For the GS configuration, we find a zero-point renormalization of −0.07 eV, while for 600 K the effect amounts to −0.22 eV. All in all, the

inclusion of (a)–(c) does not alter the striking findings of this study but merely leads to a lowering of T_c due to (c). We emphasize that vibrational effects can be consistently accounted for in our method. A short outline can be found in the SM [24]; a detailed analysis will be presented elsewhere.

To summarize, we have developed a method to obtain the temperature-dependent effective band structure of alloys. Our method can be applied to complex systems with many atoms in the primitive cell. Local atomic environments are fully accounted. Thanks to a symmetrization procedure, the resulting spectral function could be compared to angle-resolved photoemission spectra [11]. We have challenged our method by applying it to the thermoelectric clathrate alloy $Ba_8Al_{16}Si_{30}$. The configurational changes of Al atoms in the Si host structure as a function of temperature reveal a partial order-disorder phase transition. The critical temperature of this phase transition in the macroscopic limit is determined as 582 K. This transition goes hand in hand with a closing of the effective band gap, which is expected to dramatically impact the thermoelectric efficiency. As a consequence, it is anticipated that clathrate phases, annealed at different temperatures, exhibit large differences in their thermoelectric performance. A closing of the effective band gap driven by a partial order-disorder phase transition is also present in heavily n-doped clathrates, as, e.g., in compositions with 15 Al atoms in the host structure [47], and will be published elsewhere. Our results point to the crucial role of disorder in complex thermoelectric materials. Overall, we have demonstrated that a multiscale approach is needed to obtain a reliable description of the macroscopic properties for such complex materials. In particular, it is essential to capture the diverse temperature-dependent configurational effects present in those alloys rather than restricting calculations to ground-state properties and/or a few selected structures. We have further shown that a finite-size scaling is required to reach the macroscopic description at the critical point of the material's phase transition.

Input and output files can be downloaded from NOMAD [49].

M. T. acknowledges funding from the Elsa-Neumann Stiftung Berlin. We thank Oleg Rubel for drawing our attention to Refs. [9,10].

*maria.troppenz@physik.hu-berlin.de

[1] L. Bellaiche and D. Vanderbilt, Phys. Rev. B **61**, 7877 (2000).
[2] P. Soven, Phys. Rev. **156**, 809 (1967).
[3] P. Soven, Phys. Rev. B **2**, 4715 (1970).
[4] A. V. Ruban and I. A. Abrikosov, Rep. Prog. Phys. **71**, 046501 (2008).
[5] V. Raghuraman, Y. Wang, and M. Widom, Phys. Rev. B **102**, 054207 (2020).
[6] J. M. Sanchez, F. Ducastelle, and D. Gratias, Physica (Amsterdam) **128A**, 334 (1984).
[7] F. Wang and D. P. Landau, Phys. Rev. Lett. **86**, 2050 (2001).
[8] M. Troppenz, S. Rigamonti, and C. Draxl, Chem. Mater. **29**, 2414 (2017).
[9] V. Popescu and A. Zunger, Phys. Rev. Lett. **104**, 236403 (2010).
[10] V. Popescu and A. Zunger, Phys. Rev. B **85**, 085201 (2012).
[11] W. Ku, T. Berlijn, and C.-C. Lee, Phys. Rev. Lett. **104**, 216401 (2010).
[12] D. P. Landau, S.-H. Tsai, and M. Exler, Am. J. Phys. **72**, 1294 (2004).
[13] I. A. Abrikosov, S. I. Simak, B. Johansson, A. V. Ruban, and H. L. Skriver, Phys. Rev. B **56**, 9319 (1997).
[14] E. Zintl, Angew. Chem. **52**, 1 (1939).
[15] S. Paschen, V. Pacheco, A. Bentien, A. Sanchez, W. Carrillo-Cabrera, M. Baenitz, B. Iversen, Y. Grin, and F. Steglich, Physica (Amsterdam) **328B**, 39 (2003).
[16] M. Christensen, S. Johnsen, and B. B. Iversen, Dalton Trans. **39**, 978 (2010).
[17] A. V. Shevelkov and K. Kovnir, *Zintl Phases: Principles and Recent Developments* (Springer, Berlin, 2011), pp. 97–142.
[18] N. P. Blake, L. Møllnitz, G. Kresse, and H. Metiu, J. Chem. Phys. **111**, 3133 (1999).
[19] N. P. Blake, D. Bryan, S. Latturner, L. Møllnitz, G. D. Stucky, and H. Metiu, J. Chem. Phys. **114**, 10063 (2001).
[20] K. Akai, T. Uemura, K. Kishimoto, T. Tanaka, H. Kurisu, S. Yamamoto, T. Koyanagi, K. Koga, H. Anno, and M. Matsuura, J. Electron. Mater. **38**, 1412 (2009).
[21] M. Ångqvist, D. O. Lindroth, and P. Erhart, Chem. Mater. **28**, 6877 (2016).
[22] J. P. Perdew, A. Ruzsinszky, G. I. Csonka, O. A. Vydrov, G. E. Scuseria, L. A. Constantin, X. Zhou, and K. Burke, Phys. Rev. Lett. **100**, 136406 (2008).
[23] A. Gulans, S. Kontur, C. Meisenbichler, D. Nabok, P. Pavone, S. Rigamonti, S. Sagmeister, U. Werner, and C. Draxl, J. Phys. Condens. Matter **26**, 363202 (2014).
[24] See Supplemental Material at http://link.aps.org/supplemental/10.1103/PhysRevLett.130.166402, which includes Refs. [7,8,22,23,25–37], for the supplemental Figs. 1–9.
[25] S. Rigamonti, M. Troppenz, M. Kuban, A. Hübner, and C. Draxl, CELL: A PYTHON package for cluster expansion with a focus on complex alloys (to be published).
[26] CELL, https://sol.physik.hu-berlin.de/cell.
[27] S. Schnabel, D. T. Seaton, D. P. Landau, and M. Bachmann, Phys. Rev. E **84**, 011127 (2011).
[28] M. Zacharias and F. Giustino, Phys. Rev. B **94**, 075125 (2016).
[29] M. Zacharias and F. Giustino, Phys. Rev. Res. **2**, 013357 (2020).
[30] J. Kim, A. Gulans, and C. Draxl, Electron. Struct. **2**, 037001 (2020).
[31] Y. W. Tsang and M. L. Cohen, Phys. Rev. B **3**, 1254 (1971).
[32] M. Falmbigl, G. Rogl, P. Rogl, M. Kriegisch, H. Müller, E. Bauer, M. Reinecker, and W. Schranz, J. Appl. Phys. **108**, 043529 (2010).
[33] A. van de Walle and G. Ceder, Rev. Mod. Phys. **74**, 11 (2002).

[34] V. Blum, R. Gehrke, F. Hanke, P. Havu, V. Havu, X. Ren, K. Reuter, and M. Scheffler, Comput. Phys. Commun. **180**, 2175 (2009).
[35] D. Connétable, Phys. Rev. B **82**, 075209 (2010).
[36] M. Cardona, Phys. Status Solidi (a) **188**, 1209 (2001).
[37] P. Lautenschlager, P. B. Allen, and M. Cardona, Phys. Rev. B **31**, 2163 (1985).
[38] N. Metropolis, A. W. Rosenbluth, M. N. Rosenbluth, A. H. Teller, and E. Teller, J. Chem. Phys. **21**, 1087 (1953).
[39] W. K. Hastings, Biometrika **57**, 97 (1970).
[40] W. L. Bragg and E. K. Williams, Proc. R. Soc. A **145**, 699 (1934).
[41] H. A. Bethe and H. Wills, Proc. R. Soc. A **150**, 552 (1935).
[42] D. P. Landau and K. Binder, *A Guide to Monte Carlo Simulations in Statistical Physics*, 4th ed. (Cambridge University Press, Cambridge, England, 2014), Chap. 4.2.3.
[43] M. S. S. Challa, D. P. Landau, and K. Binder, Phys. Rev. B **34**, 1841 (1986).
[44] K. Binder, Rep. Prog. Phys. **50**, 783 (1987).
[45] K. Binder, Rep. Prog. Phys. **60**, 487 (1997).
[46] M. E. J. Newman and G. T. Barkema, *Monte Carlo Methods in Statistical Physics* (Clarendon Press, Oxford, 1999).
[47] Up to now, the synthesis of clathrates with the composition $Ba_8Al_xSi_{46-x}$ has been achieved for $x \leq 15$ [48]. The increase of x toward the Zintl condition $x = 16$ is expected to yield improved thermoelectric performance. Thus, further experimental studies in this direction are desired and encouraged [48].
[48] N. Tsujii, J. H. Roudebush, A. Zevalkink, C. A. Cox-Uvarov, G. Jeffery Snyder, and S. M. Kauzlarich, J. Solid State Chem. **184**, 1293 (2011).
[49] M. Troppenz, S. Rigamonti, and C. Draxl, NOMAD (2019), 10.17172/NOMAD/2019.10.29-1.